

Prespecified-Performance Kinematic Tracking Control for Aerial Manipulation

Hauzi Cao, Jiahao Shen, Zhengzhen Li, Qinquan Ren, Shiyu Zhao

Abstract—This paper studies the kinematic tracking control problem for aerial manipulators. Existing kinematic tracking control methods, which typically employ proportional-derivative feedback or tracking-error-based feedback strategies, may fail to achieve tracking objectives within specified time constraints. To address this limitation, we propose a novel control framework comprising two key components: end-effector tracking control based on a user-defined preset trajectory and quadratic programming-based reference allocation. Compared with state-of-the-art approaches, the proposed method has several attractive features. First, it ensures that the end-effector reaches the desired position within a preset time while keeping the tracking error within a performance envelope that reflects task requirements. Second, quadratic programming is employed to allocate the references of the quadcopter base and the Delta arm, while considering the physical constraints of the aerial manipulator, thus preventing solutions that may violate physical limitations. The proposed approach is validated through three experiments. Experimental results demonstrate the effectiveness of the proposed algorithm and its capability to guarantee that the target position is reached within the preset time.

Index Terms—Aerial manipulator, Prespecified performance, Kinematic tracking control, Aerial grasping, Peg-in-hole

I. INTRODUCTION

An aerial manipulator, as a composite robotic system that integrates a multirotor base with a manipulator, not only inherits the three-dimensional maneuverability of the multicopter but also extends its physical interaction capabilities through the end-effector. This unique combination of autonomous flight and precise manipulation has attracted increasing research attention. In recent years, numerous groundbreaking advances have emerged (see [1]–[3] for recent surveys), with typical applications covering aerial grasping [4], [5], contact-based inspection [6], [7], peg-in-hole operations [8], [9] (Fig 1), etc. These applications have progressively validated the practical value of the aerial manipulator.

Hauzi Cao is with the Westlake Institute for Optoelectronics and the WINDY Lab in the Department of Artificial Intelligence, Westlake University, Hangzhou 311421, China (E-mail: caohuazi@wioe.westlake.edu.cn)

Jiahao Shen, Zhengzhen Li, and Shiyu Zhao are with the WINDY Lab in the Department of Artificial Intelligence, Westlake University, Hangzhou 310024, China (E-mail: {shenjiahao, lizhengzhen, zhaoshiyu}@westlake.edu.cn).

Qinyuan Ren is with the College of Control Science and Engineering, Zhejiang University, Hangzhou 310027, China (E-mail: renqinyuan@zju.edu.cn).

This work was supported by the National Major Research & Development Plan - Intelligent Robotics Major Special Project (Grant No. 2023YFB4705500), the National Natural Science Foundation of China (Grant No. 62473320), and the Open Foundation of the National Key Laboratory of Autonomous Intelligent Unmanned Systems (Grant No. 2024-SRIAS-KF-007). (Corresponding author: Shiyu Zhao)



Fig. 1: Aerial peg-in-hole assembly by an aerial manipulator. Details are available in the supplementary video.

Developing high-accuracy control methods is essential for aerial manipulators. Current control methods for aerial manipulators primarily focus on low-level motion control and kinematic control. Low-level motion control methods leverage the aerial manipulator's dynamics to design the control law that regulates rotor speeds and manipulator joint torques. Existing low-level motion control methods can be categorized into decoupled control [10], [11] and coupled control [12], [13]. However, low-level motion control alone is not sufficient for millimeter-level precision owing to model inaccuracies and disturbance susceptibility [9]. This motivates the exploration of alternative approaches, such as kinematic control, for aerial manipulators.

Kinematic control is derived from the kinematics of aerial manipulators, focusing on achieving high-precision end-effector control through the coordination of motions of the multirotor base and the manipulator. Compared to ground-based manipulators, the kinematic control of aerial manipulators is more challenging for two reasons. First, the manipulator and the multirotor base are dynamically coupled, indicating that their motions have a mutual influence on each other. Second, aerial manipulators operate within a 3D environment rather than in a 2D environment. Moreover, most tasks necessitate 3D coordinated motion between the multirotor base and the manipulator for successful execution. Existing studies on kinematic control methods for aerial manipulators primarily focus on two aspects.

The first aspect is the control architecture. Current control architectures can be classified into two types: decoupled

architecture and coupled architecture. The decoupled architecture separately designs kinematic control for the multirotor base and the manipulator [9], [14]. It achieves end-effector control through a sequential “platform positioning first, manipulator operation second” strategy [5]. Although simple to implement, this approach suffers from low energy efficiency and slow response speed [1]. In contrast, coupled architecture treats the multirotor base and the manipulator as an integrated system [11], coordinating their movements through Jacobian matrix-based methods. Although this approach demonstrates superior energy efficiency and enhanced response characteristics, it introduces significant control complexity due to the necessity of simultaneously managing the degrees of freedom of both subsystems.

The second aspect is the feedback strategy. Since higher-order motion information of both targets and end-effectors is generally difficult to obtain, positional feedback is typically employed to implement kinematic control of aerial manipulators [15]. There are two existing feedback strategies. The first is the closed-loop inverse kinematics (CLIK) strategy, which utilizes a control law analogous to Proportional-Derivative control to achieve end-effector tracking [16]–[18]. The second strategy directly employs end-effector tracking error, typically implemented in the form of model predictive control (MPC) [19], [20]. By incorporating the end-effector tracking error into the MPC cost function, this strategy generates references for both the multirotor base and the manipulator that reduce the tracking error [4]. Although both feedback strategies can accomplish end-effector tracking, neither guarantees that the end-effector reaches the target point within the specified time.

The objective of this paper is to achieve kinematic control that enables the end-effector to complete tracking tasks within specified time constraints. The above analysis reveals the limitations in the two aspects of the existing kinematic control approaches for aerial manipulation. This paper aims to overcome these limitations by proposing a new framework that incorporates preset trajectory tracking control and quadratic programming (QP)-based trajectory allocation (see Fig. 2(a)). The proposed algorithms are verified by carefully designed experiments on an aerial manipulation platform. The novelty of the proposed algorithms is summarized below.

1) We propose a novel two-layer architecture to achieve the tracking control of the end-effector with prespecified performance. The architecture enables the aerial manipulator’s end-effector to reach the designated position within a preset time. Moreover, by incorporating the aerial manipulator’s physical constraints into the reference trajectory allocation, it prevents the aerial manipulator from oscillating at constraint boundaries. Compared with existing methods based on CLIK [21] and tracking-error feedback strategies [19], the proposed method guarantees task completion time and ensures better compliance with planned execution outcomes.

2) We propose a method for generating performance envelope boundaries according to the task completion metrics, including the initial tracking error, steady-state tracking error requirements, and convergence time. This approach enables

researchers to flexibly design the parameters of performance envelope boundaries according to actual task requirements.

3) We employ a preset tracking error trajectory to constrain the end-effector’s tracking error. Compared with existing prescribed performance control methods based on barrier functions [22], our approach effectively avoids singularity issues. In conventional methods, barrier functions are prone to generating singular phenomena under boundary conditions, which not only leads to divergence of the control law but may also cause system safety hazards [23]. In contrast, the preset tracking error trajectory method proposed in this work fundamentally eliminates the possibility of singularity occurrence, thereby significantly enhancing system safety and reliability.

II. MODELING

This section shows coordinate frames, notations, and kinematics of the aerial manipulator. It develops a kinematic model for end-effector tracking of the aerial manipulator.

A. Coordinate Frames and Notations

The aerial manipulator has three reference frames: the inertial frame Σ_I , the quadcopter body-fixed frame Σ_B , and the Delta arm frame Σ_D (see Fig. 2(a)). Σ_I is an inertial frame where the z -axis is in the direction of the gravity vector. Σ_B is rigidly attached to the quadcopter base. Its origin coincides with the center of gravity of the quadcopter. Σ_D is rigidly attached to the Delta arm base at its geometric center $\mathbf{p}_C \in \mathbb{R}^3$.

Denote the position of the end-effector in Σ_I as $\mathbf{p}_E \in \mathbb{R}^3$. Let $\mathbf{p}_O \in \mathbb{R}^3$ denote the object position in Σ_I . Then, the tracking error of the end-effector is $\mathbf{e}_E = \mathbf{p}_E - \mathbf{p}_O = [e_{E,x}, e_{E,y}, e_{E,z}]^T \in \mathbb{R}^3$. To clearly represent the Cartesian components of vectors, we define $\nu \in \{x, y, z\}$ as the component index. For instance, the components of the tracking error vector \mathbf{e}_e can be expressed as $e_{E,\nu}$, where $\nu \in \{x, y, z\}$.

B. Kinematics of the Aerial Manipulator

The aerial manipulator analyzed in this paper comprises a quadcopter base and a Delta arm (see Fig. 2(a)). The Delta arm’s end-effector position can translate relative to the base, while its orientation remains aligned with the base orientation. Denote the position of the quadcopter base in Σ_I as $\mathbf{p}_B \in \mathbb{R}^3$. Let $\mathbf{R}_B \in SO(3)$ denote the rotation matrix from Σ_B to Σ_I . The kinematic expression for the aerial manipulator can then be written as $\mathbf{p}_E = \mathbf{p}_B + \mathbf{R}_B \mathbf{p}_E^B$, where, $\mathbf{p}_E^B \in \mathbb{R}^3$ represents the position of the end-effector in Σ_B , which can be obtained through the forward kinematics of the manipulator.

Let $\mathbf{p}_C^B \in \mathbb{R}^3$ denote the position of the center of the base in Σ_B . Let $\mathbf{p}_E^D \in \mathbb{R}^3$ denote the position of the end-effector in Σ_D . The relationship between \mathbf{p}_E^B and \mathbf{p}_E^D is $\mathbf{p}_E^B = \mathbf{R}_D^B \mathbf{p}_E^D + \mathbf{p}_C^B$, where $\mathbf{R}_D^B \in SO(3)$ is the rotation matrix from Σ_D to Σ_B . \mathbf{p}_E^D is a function of the joint angle vector $\mathbf{q} = [q_1, q_2, q_3]^T$, and the function can be found in [24].

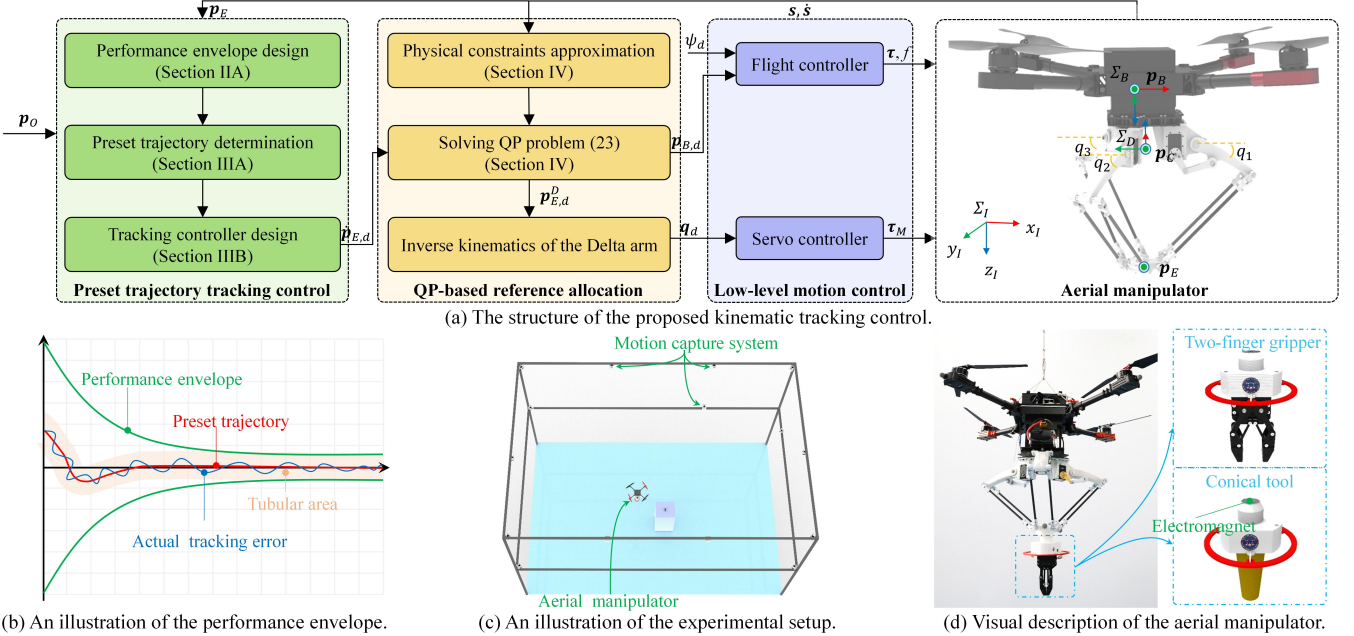


Fig. 2: The system overview, the preset envelope, and experimental setup of the aerial manipulator system.

As can be seen from Fig. 2(a), the joint angles of the Delta arm are driven by planar four-bar linkages. The relationship between the joint angles and the crank position angles can be calculated by the kinematics of the planar four-bar linkage [25, Section 3.6].

III. PRESET TRAJECTORY TRACKING CONTROL

This section proposes a preset trajectory kinematic tracking control method. It ensures that the end-effector reaches the desired position within a preset time while keeping the tracking error within a performance envelope.

A. Performance Envelope

The performance envelope is introduced to represent the performance criterion of the aerial manipulator. The boundary function of the performance envelope is denoted as $\rho(t) \in \mathbb{R}^3$. According to [23], we employ a boundary function with an exponential form to ensure that the absolute value of the tracking error gradually decreases. The boundary function is designed to $\rho_\nu(t) = (\rho_{\nu,0} - \rho_{\nu,\infty}) \exp(-l_E t) + \rho_{\nu,\infty} \in \mathbb{R}$, where $\nu \in \{x, y, z\}$. Here, $\rho_0 = [\rho_{x,0}, \rho_{y,0}, \rho_{z,0}]^T \in \mathbb{R}^3$, $\rho_\infty = [\rho_{x,\infty}, \rho_{y,\infty}, \rho_{z,\infty}]^T \in \mathbb{R}^3$, and l_E are positive parameters of the boundary function.

The parameters of the boundary function are determined by analyzing task completion metrics, including the initial tracking error, steady-state tracking error requirements, and convergence time. Specifically, ρ_0 relates to the initial tracking error, requiring that $\rho_{\nu,0} > |e_{E,\nu}(0)|$, where $\nu \in \{x, y, z\}$, the definition of $e_{E,\nu}$ can be seen in Section II-A. The parameter ρ_∞ represents the maximum allowable steady-state tracking error. Its lower bound is typically determined by the end-effector's achievable steady-state tracking accuracy, while the upper bound is determined by the operational

precision requirements of the actual tasks. The parameter l_E is the decay rate of the performance function. It can be determined in two steps. The first is to determine a tolerance threshold for the preset trajectory. The exponential decay process of $\rho(t)$ exhibits a monotonic decrease toward its asymptotic steady-state value ρ_∞ . The preset time $t_p \in \mathbb{R}$ is defined as the time required for the tracking error to converge to within $\pm \rho_\infty$. It is constrained by the maximum speed of the aerial manipulator's end-effector. We let $\epsilon_p \in \mathbb{R}$ as the tolerance threshold, and its definition is

$$\epsilon_p = (\|\rho_0\| - \|\rho_\infty\|) e^{-l_E t_p}. \quad (1)$$

In practical implementations, ϵ_p can be determined by a scalar multiple of $\|\rho_\infty\|$, such as $0.1\|\rho_\infty\|$, to align with task completion metrics. The second is to calculate the parameter l_E with the value of ϵ_p . According to (1), we have $l_E = \ln[(\|\rho_0\| - \|\rho_\infty\|)/\epsilon_p]/t_p$.

B. Preset Tracking Error Trajectory

The preset tracking error trajectory of the end-effector is introduced to constrain the end-effector's tracking error. Through the tracking controller in Section III-C, the actual tracking error is constrained to track the preset trajectory, guaranteeing its strict containment within the performance envelope (see Fig. 2(b)). Let $\alpha(t) = [\alpha_x(t), \alpha_y(t), \alpha_z(t)]^T \in \mathbb{R}^3$ denote the preset trajectory. Let $c = [c_x, c_y, c_z]^T \in \mathbb{R}^3$ denote the design parameter vector of $\alpha(t)$. To ensure the preset trajectory is monotonically decreasing and contained within the performance envelope, it is designed as $\dot{\alpha}_\nu(t) = -l_E \alpha_\nu(t) + b_\nu e^{-(l_E + c_\nu)t}$, $\alpha_\nu(0) = e_{E,\nu}(0)$, $\nu \in \{x, y, z\}$, where $b_\nu > 0$ is determined by (20), and $b_\nu = l_E e_{E,\nu}(0) + \dot{e}_{E,\nu}(0) \in \mathbb{R}$. The solution of $\alpha_\nu(t)$ is

$$\alpha_\nu(t) = \frac{b_\nu}{c_\nu} (1 - e^{-c_\nu t}) e^{-l_E t} + e_{E,\nu}(0) e^{-l_E t}. \quad (2)$$

From (2), we have $\alpha_\nu(0) = e_{E,\nu}(0)$ and $\alpha_\nu(\infty) = 0$. The preset trajectory is initialized with the initial tracking error and converges to zero at its terminal value. The first and second time derivatives of $\alpha_\nu(t)$ are

$$\dot{\alpha}_\nu(t) = \frac{b_\nu}{c_\nu} [-l_E e^{-l_E t} + (c_\nu + l_E) e^{-(c_\nu + l_E)t}] - e_{E,\nu}(0) l_E e^{-l_E t}, \quad (3)$$

$$\ddot{\alpha}_\nu(t) = \frac{b_\nu}{c_\nu} [l_E^2 e^{-l_E t} - (c_\nu + l_E)^2 e^{-(c_\nu + l_E)t}] + e_{E,\nu}(0) l_E^2 e^{-l_E t}. \quad (4)$$

Lemma 1: Let ε_ν be a positive constant satisfying $\varepsilon_\nu < \min\{\rho_{\nu,\infty}, \rho_{\nu,0} - |e_{E,\nu}(0)|\}$, where $\nu \in \{x, y, z\}$. For the preset trajectory of the tracking error calculated by (2), if $c_\nu > b_\nu/(\rho_{\nu,0} - \varepsilon_\nu - |e_{E,\nu}(0)|)$ such that $|\alpha_\nu(t)| < \rho_\nu(t) - \varepsilon_\nu, \forall t \geq 0$.

Proof: Define $\gamma_\nu(t) = \rho_\nu(t) - \varepsilon_\nu - |\alpha_\nu(t)|$, we have

$$\begin{aligned} \gamma_\nu(t) &= (\rho_{\nu,0} - \rho_{\nu,\infty}) e^{-l_E t} + \rho_{\nu,\infty} - \varepsilon_\nu \\ &\quad - \left| e_{E,\nu}(0) e^{-l_E t} + \frac{b_\nu}{c_\nu} [1 - e^{-c_\nu t}] e^{-l_E t} \right| \\ &\geq \left[\rho_{\nu,0} - \varepsilon_\nu - |e_{E,\nu}(0)| - \frac{|b_\nu|}{c_\nu} (1 - e^{-c_\nu t}) \right] e^{-l_E t} \\ &\quad + \rho_{\nu,\infty} (1 - e^{-l_E t}) - \varepsilon_\nu + \varepsilon_\nu e^{-l_E t}. \\ &= \left[\rho_{\nu,0} - \varepsilon_\nu - |e_{E,\nu}(0)| - \frac{|b_\nu|}{c_\nu} (1 - e^{-c_\nu t}) \right] e^{-l_E t} \\ &\quad + (\rho_{\nu,\infty} - \varepsilon_\nu) (1 - e^{-l_E t}). \end{aligned} \quad (5)$$

From (5), one can conclude that if $\rho_{\nu,0} - |e_{E,\nu}(0)| - |b_\nu|/c_\nu > 0$ and $\rho_{\nu,\infty} > \varepsilon_\nu$, then $\gamma_\nu > 0$. According to the definition of ε_ν , $\rho_{\nu,\infty} > \varepsilon_\nu$ is naturally satisfied. Therefore, if we let $c_\nu > |b_\nu|/(\rho_{\nu,0} - \varepsilon_\nu - |e_{E,\nu}(0)|)$, then we have $\gamma_\nu > 0$. From the definition of $\gamma_\nu(t)$, we have $|\alpha_\nu(t)| < \rho_\nu(t) - \varepsilon_\nu, \forall t \geq 0$. This completes the proof. \square

Lemma 1 gives a method to determine the parameter vector c . Through the regulation of c , the descent rate of the preset trajectory is made faster than that of the performance envelope boundary function, thereby guaranteeing the tracking error contained within the performance envelope.

C. Tracking Control Design

The goal of tracking control is to compute the desired end-effector velocity command $\dot{\mathbf{p}}_{E,d}$ such that the end-effector position \mathbf{p}_E tracks the target position \mathbf{p}_O . In order to ensure that the tracking error satisfies the requirements of the performance envelope, we introduce the preset trajectory for the tracking error into the tracking control design (see Fig. 2b). This ensures that the end-effector of the manipulator can track \mathbf{p}_O within the preset time.

Let $\mathbf{z} = \mathbf{e}_E - \dot{\mathbf{a}}(t)$. The sliding mode vector is defined as

$$\mathbf{s} = \mathbf{z} + \mathbf{\Lambda} \int_0^t \mathbf{z} dt, \quad (6)$$

where $\mathbf{\Lambda}$ is a positive diagonal matrix. Then, we have

$$\dot{\mathbf{s}} = \dot{\mathbf{z}} + \mathbf{\Lambda} \mathbf{z} = \dot{\mathbf{p}}_E - \dot{\mathbf{p}}_O - \dot{\mathbf{a}} + \mathbf{\Lambda} \mathbf{z}. \quad (7)$$

The relationship between the actual velocity and the desired velocity input given to the controller can be described as

$$\dot{\mathbf{p}}_E = \dot{\mathbf{p}}_{E,d} + \mathbf{\Delta}, \quad (8)$$

where $\mathbf{\Delta}$ represents an unknown item. Equation (8) reflects the capability of reference allocation of the aerial manipulator, since the objective of reference allocation is to ensure that $\dot{\mathbf{p}}_E$ accurately tracks $\dot{\mathbf{p}}_{E,d}$. Substituting (8) into (7) yields

$$\dot{\mathbf{s}} = \dot{\mathbf{p}}_{E,d} + \mathbf{\Delta} - \dot{\mathbf{p}}_O - \dot{\mathbf{a}} + \mathbf{\Lambda} \mathbf{z}. \quad (9)$$

The tracking control law is designed as

$$\dot{\mathbf{p}}_{E,d} = \dot{\mathbf{p}}_O + \dot{\mathbf{a}} - \mathbf{\Lambda} \mathbf{z} - \mathbf{K} \mathbf{s}, \quad (10)$$

where \mathbf{K} is the gain matrix, and it is a positive diagonal matrix.

Theorem 1: Assuming that $\mathbf{\Delta}$ is bounded, i.e., $\|\mathbf{\Delta}\| \leq \delta_E$, if the tracking control law is designed as (10), then the position error \mathbf{e}_E is bounded and $|\mathbf{e}_{E,\nu}| < \rho_\nu(t), \forall t \geq 0$.

Proof: A candidate Lyapunov function is given as $V_E(\mathbf{s}) = \frac{1}{2} \mathbf{s}^T \mathbf{s}$. The time derivative of V_E is given as

$$\begin{aligned} \dot{V}_E &= \mathbf{s}^T (\dot{\mathbf{p}}_E - \dot{\mathbf{p}}_O - \dot{\mathbf{a}} + \mathbf{\Lambda} \mathbf{z}). \\ &= \mathbf{s}^T (\dot{\mathbf{p}}_{E,d} - \mathbf{\Delta} - \dot{\mathbf{p}}_O - \dot{\mathbf{a}} + \mathbf{\Lambda} \mathbf{z}). \end{aligned} \quad (11)$$

Substituting (10) into (11) yields $\dot{V}_E = -\mathbf{s}^T \mathbf{K} \mathbf{s} - \mathbf{s}^T \mathbf{\Delta}$. Using the comparison theorem [26, Section 9.3], we define $W = \sqrt{V_E} = \|\mathbf{s}\|/\sqrt{2}$. Then, we have

$$\begin{aligned} \dot{W} &= \frac{-\mathbf{s}^T \mathbf{K} \mathbf{s} - \mathbf{s}^T \mathbf{\Delta}}{\sqrt{2} \|\mathbf{s}\|} \\ &\leq \frac{-\lambda_{\min}(\mathbf{K}) \|\mathbf{s}\|^2 + \delta_E \|\mathbf{s}\|}{\sqrt{2} \|\mathbf{s}\|} \\ &= -\lambda_{\min}(\mathbf{K}) W + \delta_E / \sqrt{2}, \end{aligned} \quad (12)$$

where $\lambda_{\min}(\mathbf{K})$ is the minimum eigenvalue of \mathbf{K} . Since \mathbf{K}_v is a positive diagonal matrix, we have $\lambda_{\min}(\mathbf{K}) > 0$. Then, we have

$$W(t) \leq W(0) e^{-\lambda_{\min}(\mathbf{K}) t} + \delta_E / (\sqrt{2} \lambda_{\min}(\mathbf{K})). \quad (13)$$

Since $W(0) = 0$, one can obtain

$$W(t) \leq \delta_E / (\sqrt{2} \lambda_{\min}(\mathbf{K})). \quad (14)$$

According to the definition of W , we have $\|\mathbf{s}\| \leq \delta_E / \lambda_{\min}(\mathbf{K})$.

Let $\mathbf{z}_f = \int_0^t \mathbf{z} dt$ denote the integral of \mathbf{z} with respect to time. According to (6), we have

$$\dot{\mathbf{z}}_f = -\mathbf{\Lambda} \mathbf{z}_f + \mathbf{s}. \quad (15)$$

Combining (15) and $\mathbf{z}_f(0) = 0$ yields

$$\begin{aligned} \mathbf{z}_f &= \mathbf{z}_f(0) e^{-\mathbf{\Lambda} t} + \int_0^t e^{-\mathbf{\Lambda}(t-\tau)} \mathbf{s}(\tau) d\tau \\ &= \int_0^t e^{-\mathbf{\Lambda}(t-\tau)} \mathbf{s}(\tau) d\tau \end{aligned} \quad (16)$$

Therefore, we have

$$\begin{aligned}\|\mathbf{z}_f\| &\leq \frac{\delta_E}{\lambda_{\min}(\mathbf{K})} \int_0^t e^{-\lambda_{\min}(\mathbf{\Lambda})(t-\tau)} d\tau \\ &= \delta_E (1 - e^{-\lambda_{\min}(\mathbf{\Lambda})t}) / (\lambda_{\min}(\mathbf{K}) \lambda_{\min}(\mathbf{\Lambda})) \\ &\leq \delta_E / (\lambda_{\min}(\mathbf{K}) \lambda_{\min}(\mathbf{\Lambda})).\end{aligned}\quad (17)$$

According to the definition of \mathbf{s} , one can obtain that

$$\begin{aligned}\|\mathbf{z}\| - \|\mathbf{\Lambda z}_f\| &\leq \|\mathbf{z}\| - \|\mathbf{\Lambda z}_f\| \leq \|\mathbf{z} + \mathbf{\Lambda z}_f\| \\ &= \|\mathbf{s}\| \leq \delta_E / \lambda_{\min}(\mathbf{K}).\end{aligned}\quad (18)$$

Let δ_z denote the upper bound of $\|\mathbf{z}\|$. From (17) and (18), one can conclude that

$$\begin{aligned}\|\mathbf{z}\| &\leq \|\mathbf{\Lambda z}_f\| + \delta_E / \lambda_{\min}(\mathbf{K}) \\ &\leq \frac{(\lambda_{\min}(\mathbf{\Lambda}) + \lambda_{\max}(\mathbf{\Lambda})) \delta_E}{\lambda_{\min}(\mathbf{\Lambda}) \lambda_{\min}(\mathbf{K})} = \delta_z.\end{aligned}\quad (19)$$

Further, we prove that $|e_{E,\nu}| \leq \rho_\nu(t)$, $\nu \in \{x, y, z\}$ by two steps. First, the parameter c_ν is determined according to Lemma 1. The gain matrix \mathbf{K} is chosen such that $\delta_z < \min\{\rho_{\nu,\infty}, \rho_{\nu,0} - |e_{E,\nu}(0)|\}$. The parameters c_ν is chosen as

$$c_\nu > b_\nu / (\rho_{\nu,0} - \delta_z - |e_{E,\nu}(0)|), \nu \in \{x, y, z\}. \quad (20)$$

From Lemma 1, we have

$$|\alpha_\nu(t)| < \rho_\nu(t) - \delta_z, \forall t \geq 0 \text{ and } \nu \in \{x, y, z\}. \quad (21)$$

Second, the upper bound of $|e_{E,\nu}|$ is obtained from its definition and the upper bound of $|\alpha_\nu(t)|$. Since $|e_{E,\nu}| = |e_{E,\nu} - \alpha_\nu + \alpha_\nu| \leq \|\mathbf{z}\| + |\alpha_\nu|, \forall t \geq 0$, we have

$$|e_{E,\nu}| < \delta_z + \alpha_\nu, \forall t \geq 0. \quad (22)$$

By comparing (21) and (22), one can conclude that $|e_{E,\nu}| < \rho_\nu(t), \forall t \geq 0$. This completes the proof. \square

IV. REFERENCE ALLOCATION

This section proposes a reference allocation method to coordinate the quadcopter base and the Delta arm to track $\dot{\mathbf{p}}_{E,d}$ derived from (10). In addition, physical constraints are considered in the proposed method to avoid solutions that may violate physical constraints, rendering them impractical for the aerial manipulator. The considered physical constraints of the aerial manipulator include position, velocity, and acceleration constraints.

Let $\mathbf{s} = [\mathbf{p}_B^T, \mathbf{p}_E^{D,T}]^T$ denote the state of the aerial manipulator, which consists of the position of the quadcopter base in Σ_I and the position of the end-effector in Σ_D . Then, the time derivative of \mathbf{p}_E is $\dot{\mathbf{p}}_E = \mathbf{J}\dot{\mathbf{s}} - [\mathbf{R}_B \mathbf{p}_E^B]_{\times} \boldsymbol{\omega}$, where $\mathbf{J} = [\mathbf{I}_3, \mathbf{R}_B \mathbf{R}_D^B]$ is the Jacobian matrix, \mathbf{I}_3 is the 3×3 identity matrix.

To calculate the references of the quadcopter base and the Delta arm with the given desired end-effector position, the reference allocation problem is mathematically formulated as a QP problem:

$$\begin{aligned}\min_{\dot{\mathbf{s}}} \quad & F(\dot{\mathbf{s}}) = (\dot{\mathbf{p}}_E - \dot{\mathbf{p}}_{E,d})^T (\dot{\mathbf{p}}_E - \dot{\mathbf{p}}_{E,d}) + \dot{\mathbf{s}}^T \mathbf{W} \dot{\mathbf{s}} \\ &= \dot{\mathbf{s}}^T (\mathbf{J}^T \mathbf{J} + \mathbf{W}) \dot{\mathbf{s}} \\ &\quad - 2(\dot{\mathbf{p}}_{E,d} + [\mathbf{R}_B \mathbf{p}_E^B]_{\times} \boldsymbol{\omega})^T \mathbf{J} \dot{\mathbf{s}} \\ \text{s.t.} \quad & \dot{\mathbf{s}}_{\underline{p}} \leq \dot{\mathbf{s}} \leq \dot{\mathbf{s}}_{\bar{p}}, \dot{\mathbf{s}}_{\min} \leq \dot{\mathbf{s}} \leq \dot{\mathbf{s}}_{\max}, \dot{\mathbf{s}}_{\underline{v}} \leq \dot{\mathbf{s}} \leq \dot{\mathbf{s}}_{\bar{v}},\end{aligned}\quad (23)$$

where $F(\dot{\mathbf{s}})$ is the cost function of the QP problem, \mathbf{W} is a positive diagonal matrix, $\dot{\mathbf{p}}_{E,d}$ is calculated by (10), $\dot{\mathbf{s}}_{\underline{p}}$ and $\dot{\mathbf{s}}_{\bar{p}}$ are lower and upper approximate bounds of the actuated state position. $\dot{\mathbf{s}}_{\min}$ and $\dot{\mathbf{s}}_{\max}$ are the upper and lower bounds of $\dot{\mathbf{s}}$. $\dot{\mathbf{s}}_{\underline{v}}$ and $\dot{\mathbf{s}}_{\bar{v}}$ are lower and upper approximate bounds of the actuated state acceleration.

In Equation (23), if position and acceleration constraints were directly described using terms of \mathbf{s} and $\dot{\mathbf{s}}$, the QP formulation would require 18 optimization variables. To reduce computational complexity, we approximate both position and acceleration constraints as expressions represented by velocity $\dot{\mathbf{s}}$, thereby decreasing the number of variables to 6. The analytical expressions for $\dot{\mathbf{s}}_{\underline{p}}$, $\dot{\mathbf{s}}_{\bar{p}}$, $\dot{\mathbf{s}}_{\underline{v}}$, and $\dot{\mathbf{s}}_{\bar{v}}$ can be derived from Section VI-A of [11]. Let $\dot{\mathbf{s}}^* \in \mathbb{R}^6$ denote the optimal solution of QP problem (23). The constraints in (23) ensure the optimal solution $\dot{\mathbf{s}}^*$ to satisfy the physical constraints of the aerial manipulator. The desired state vector, $\mathbf{s}_d = [\mathbf{p}_{B,d}^T, \mathbf{p}_{E,d}^{D,T}]^T$, is obtained by integrating the optimal velocity solution, $\dot{\mathbf{s}}_d = \dot{\mathbf{s}}^*$. Consequently, the desired positions $\mathbf{p}_{B,d}$ and $\mathbf{p}_{E,d}^D$ can be derived from \mathbf{s}_d . The desired joint configuration \mathbf{q}_d is then calculated using the inverse kinematics of the Delta arm.

The QP problem is solved by an efficient solver, OSQP [27]. To accelerate the QP problem solution, the result from the previous iteration is used as the initial value for the next iteration. Similar to CLIK, the proposed method also enables redundancy management in prioritized multi-task scenarios. This is achieved through configurable approaches in the QP formulation, either by adding constraint conditions for hard priority enforcement or incorporating additional terms in the cost function for soft priority adjustment [19].

V. EXPERIMENTAL VERIFICATION

This section presents experimental results to verify the effectiveness of the proposed algorithms. First of all, we describe the experimental setup. The motor-to-motor distance of the quadcopter base is 0.65 m. The mass of the quadcopter (including a battery) is 3.60 kg. The Delta arm consists of a mounting base (0.56 kg) and a movable robotic arm (0.44 kg). The proposed tracking controller and the inverse kinematics of the Delta arm run on an onboard Intel NUC i7 computer with ROS. An ESO-based nonlinear controller is used as the flight controller for the quadcopter, running on a Pixhawk 4 autopilot [11]. The controller inputs include the desired position $\mathbf{p}_{B,d}$ and the desired yaw angle ψ_d . Real-world experiments utilized a Vicon motion capture system to measure the quadcopter base and end-effector positions with high accuracy (see Fig. 2c).

In all the experiments, we use the same set of control gains: $\mathbf{\Lambda} = \text{diag}([0.2, 0.2, 0.2])$, $\mathbf{K} = \text{diag}([1.2, 1.2, 1.2])$, $\delta_E = 0.01$. Parameter ρ_0 is configured according to the initial tracking error of each experiment. Parameter ρ_∞ is set as [0.02, 0.02, 0.02] for all experiments in this paper.

A. Example 1: Static Point Tracking

The goal of this experiment is to rapidly maneuver the end-effector from a start position $[0, 0, -2.1]$ m to an end

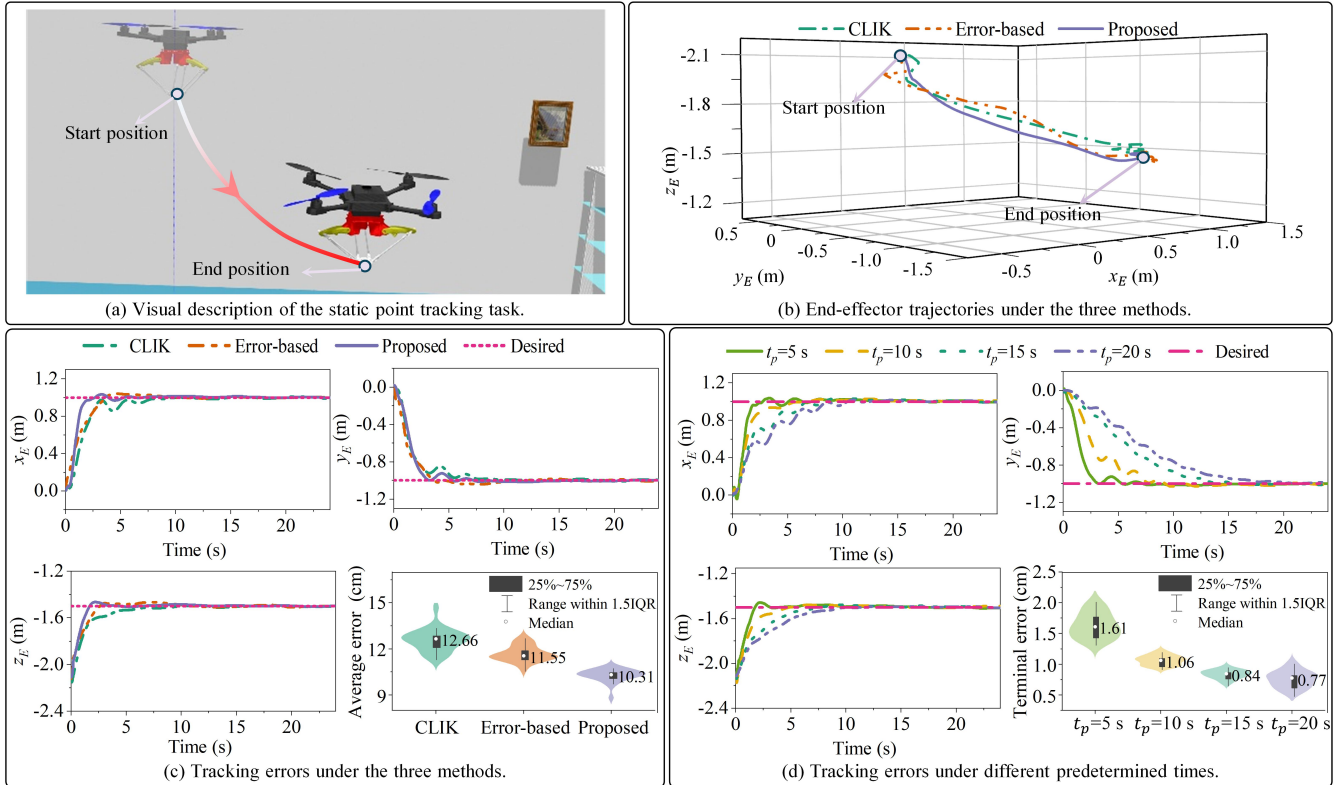


Fig. 3: Experiment results of the static point tracking example.

position $[1, -1, -1.5]$ m. This task demonstrates the accuracy and responsiveness of the proposed control algorithm. We simulate this task because many real-world applications (e.g., aerial grasping and peg-in-hole assembly) can be decomposed into point-to-point motion problems. Thus, achieving high-precision static point tracking is critical for aerial manipulators. The simulation was performed in Gazebo 11 (Fig. 3(a)), considering sensor noises (GPS, gyroscope, and accelerometer). All sensor noises are modeled as zero-mean Gaussian processes with standard deviations of 0.01 cm for GPS noise, 0.02 rad/s² for gyroscope noise, and 0.04 m/s² for accelerometer noise.

To demonstrate the advantages of the proposed algorithm, we compare the proposed method with two methods: the CLIK method and the error-based method. The CLIK method is formed by combining the CLIK feedback strategy from [28] with our proposed QP-based reference allocation. The error-based method directly utilizes the end-effector tracking error in conjunction with MPC. In the proposed method, parameters ρ_0 and c are set as $[2.0, 2.0, 1.2]$ and $[0.25, 0.25, 0.25]$, respectively. Fig. 3(b) and (c) present the comparative results. Twenty-one simulations per method were conducted to evaluate the tracking performance of the three methods. Fig. 3(c) presents the median values of average tracking errors for each method. The proposed method demonstrated superior performance with a median error of 10.31 cm (standard deviation: 0.45 cm), representing 22.8% and 12.0% reductions compared to the CLIK method (12.66 cm, standard deviation: 0.75 cm) and error-based method (11.55 cm,

standard deviation: 0.52 cm), respectively. The reason for the relatively large average tracking error is that the initial point is far from the target position. Furthermore, it demonstrated faster convergence with a median time of 2.4s, outperforming both the CLIK (4.8s) and error-based (3.2s) methods.

To further investigate the influence of the preset time t_p on the results, we perform simulations with different preset time values: 5s, 10s, 15s, and 20s. The simulation results are shown in Fig. 3(d). It can be observed that increasing the preset time reduces the tracking error in the terminal phase. To conduct a more detailed analysis, we performed 21 simulations for each of these four values. We define the terminal tracking error as the average error within five seconds after $\|e_E\| \leq \|\rho_\infty\|$. The statistical results show that by increasing the preset time from 5 to 20s, the terminal tracking error decreases from 1.61 cm to 0.77 cm.

B. Example 2: Aerial Grasping

The goal of this experiment is to grasp a target object on a pillar. In the experiment, t_p , ρ_0 , and c are set as 10s, $[0.1, 5.0, 3.0]$, and $[0.15, 0.15, 0.15]$, respectively. The start position of the end-effector is set as $[0.01, 0.99, -2.42]$ m. The position of the target object is set as $[0, -1.36, -1.34]$ m. To achieve target object grasping, a rigid two-finger gripper is mounted on the end effector (see Fig. 2d). The visual description of the experiment is shown in Fig 4(a).

The experiment demonstrates that our proposed method is capable of achieving aerial grasping. Fig 4(b-d) illustrates the results of the experiment. The 3D trajectory of the end

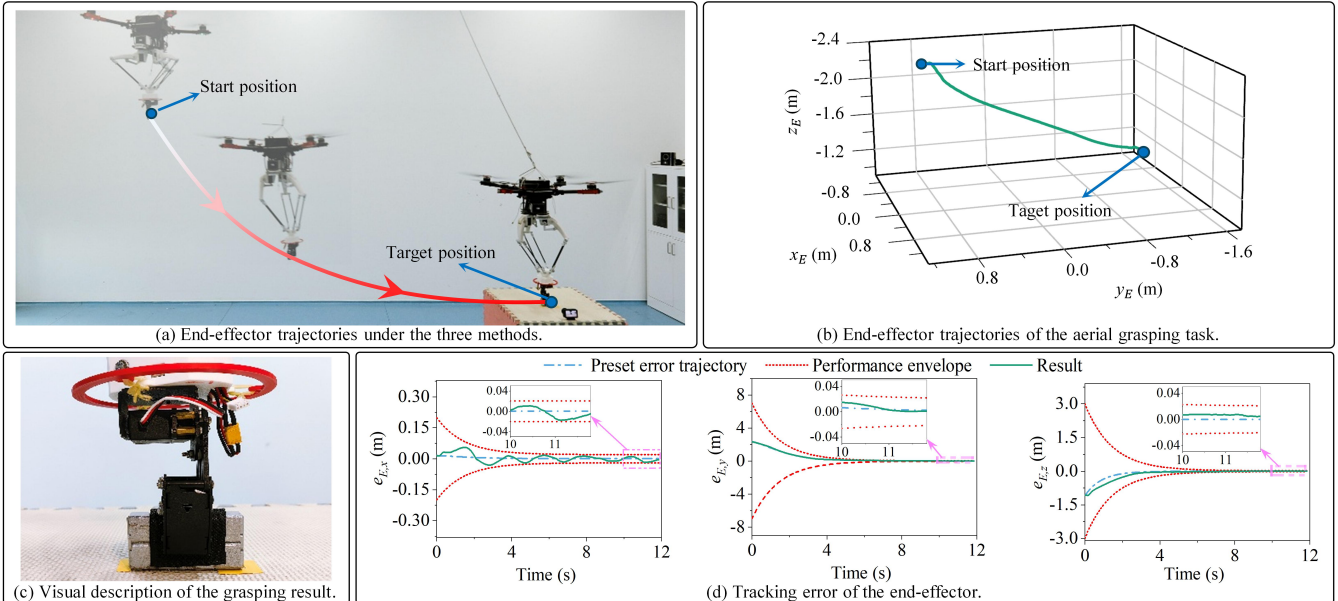


Fig. 4: Experiment results of the aerial grasping example.

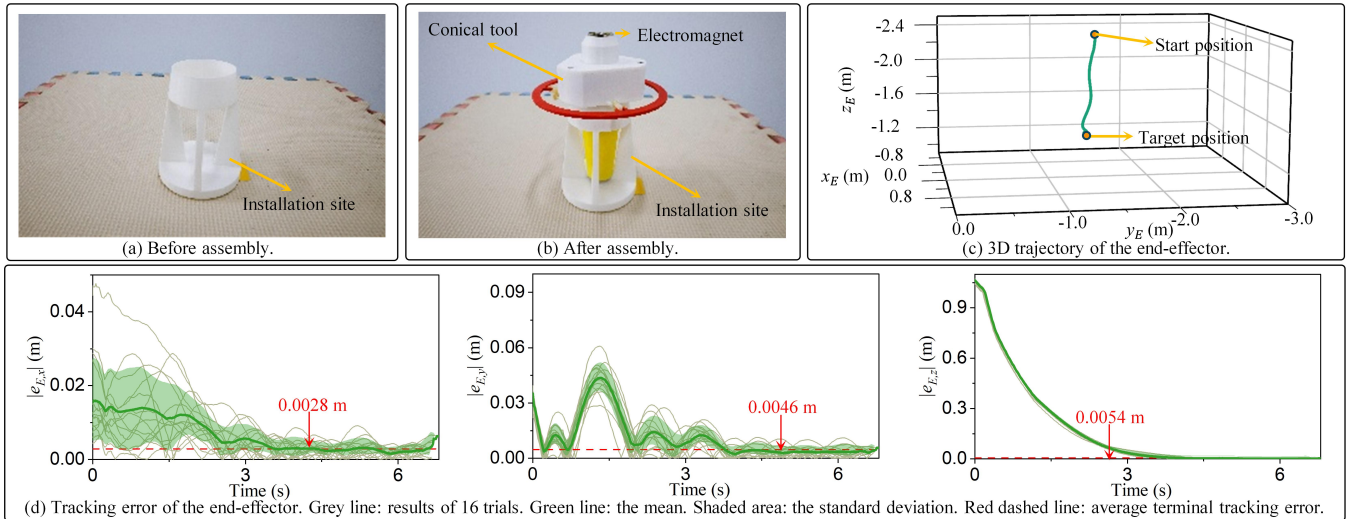


Fig. 5: Experiment results of the peg-in-hole assembly example.

effector is shown in Fig 4(b). Fig 4(c) gives the visual description of the grasping result. The tracking errors of the end-effector are given in Fig 4(d). The results show that the tracking errors in all three directions are contained within the performance envelope. The terminal tracking error of the proposed method in this experiment is 1.26 cm (standard deviation: 0.81 cm). The total task completion time was 11.8s.

C. Example 3: Peg-in-hole Assembly

The goal of this experiment is to perform a peg-in-hole assembly of a conical tool into an installation site. An electromagnet is mounted directly above the tool, enabling controllable tool attachment and detachment (see Fig. 2d). In the experiment, t_p , ρ_0 , and c are set as 5s, [0.1, 0.1, 2.0], and [0.3, 0.3, 0.3], respectively. The start position of

the end effector is [0.04, -1.47, -2.40] m, and the position of the installation site is [0.04, -1.37, -1.34] m. The visual description of the experiment is shown in Fig. 1.

The experiment demonstrates that our proposed method is capable of achieving aerial peg-in-hole assembly. Before assembly, the installation site is mounted on a pillar (Fig. 5(a)). After assembly, the tool is inserted into the installation site (Fig. 5(b)). The tracking results of the end-effector are shown in Fig. 5(c) and (d). The 16 experimental trials exhibited durations ranging from 6.2 to 6.8s, with a mean completion time of 6.5s. The average terminal tracking errors of the proposed method in the three directions are 0.28 cm, 0.46 cm, and 0.54 cm, respectively. The overall average terminal tracking error in three directions was 0.89 cm, and the standard deviation was 0.64 cm.

VI. CONCLUSION

This paper proposes a novel kinematic tracking control method composed of preset trajectory tracking control and QP-based reference allocation. Its performance was validated through three experiments. In the static point tracking experiment, comparative results demonstrate that the proposed method achieves a 22.8% reduction in average tracking error relative to the CLIK method and a 12.0% reduction compared to the error-based method. Furthermore, it is observed that adjusting the preset time t_p can effectively reduce the terminal tracking error of the end-effector. The experimental results from both aerial grasping and peg-in-hole assembly tasks demonstrate that the proposed algorithm is capable of being effectively applied to real-world aerial manipulation scenarios. Future research can focus on the following directions: (1) employing disturbance estimation methods (e.g., offline-trained neural networks [29]) to estimate Δ for improving the system's robustness against dynamic coupling and wind disturbances, and (2) implementing redundancy management strategies to enhance task completion capability.

REFERENCES

- [1] A. Ollero, M. Tognon, A. Suarez, D. Lee, and A. Franchi, "Past, present, and future of aerial robotic manipulators," *IEEE Transactions on Robotics*, vol. 38, no. 1, pp. 626–645, 2021.
- [2] X. Ding, P. Guo, K. Xu, and Y. Yu, "A review of aerial manipulation of small-scale rotorcraft unmanned robotic systems," *Chinese Journal of Aeronautics*, vol. 32, no. 01, pp. 203–217, 2019.
- [3] F. Ruggiero, V. Lippiello, and A. Ollero, "Aerial manipulation: A literature review," *IEEE Robotics and Automation Letters*, vol. 3, no. 3, pp. 1957–1964, 2018.
- [4] W. Luo, J. Chen, H. Ebel, and P. Eberhard, "Time-optimal handover trajectory planning for aerial manipulators based on discrete mechanics and complementarity constraints," *IEEE Transactions on Robotics*, vol. 39, no. 6, pp. 4332–4349, 2023.
- [5] H. Cao, J. Shen, C. Liu, B. Zhu, and S. Zhao, "Motion planning for aerial pick-and-place with geometric feasibility constraints," *IEEE Transactions on Automation Science and Engineering*, vol. 22, no. 1, pp. 2577–2594, 2025.
- [6] K. Bodie, M. Brunner, M. Pantic, S. Walser, P. Pfändler, U. Angst, R. Siegwart, and J. Nieto, "Active interaction force control for contact-based inspection with a fully actuated aerial vehicle," *IEEE Transactions on Robotics*, vol. 37, no. 3, pp. 709–722, 2020.
- [7] X. Guo, G. He, M. Mousaei, J. Geng, G. Shi, and S. Scherer, "Aerial interaction with tactile sensing," in *2024 IEEE International Conference on Robotics and Automation (ICRA)*, pp. 1576–1582, IEEE, 2024.
- [8] J. Lee, R. Balachandran, K. Kondak, A. F. Coelho, M. De Stefano, M. Humt, J. Feng, T. Asfour, and R. Triebel, "Virtual reality via object pose estimation and active learning: Realizing telepresence robots with aerial manipulation capabilities," *Field Robotics*, vol. 3, pp. 323–367, 2023.
- [9] M. Wang, Z. Chen, K. Guo, X. Yu, Y. Zhang, L. Guo, and W. Wang, "Millimeter-level pick and peg-in-hole task achieved by aerial manipulator," *IEEE Transactions on Robotics*, 2023.
- [10] M. Fumagalli, R. Naldi, A. Macchelli, F. Forte, A. Q. Keemink, S. Stramigioli, R. Carloni, and L. Marconi, "Developing an aerial manipulator prototype: Physical interaction with the environment," *IEEE robotics & automation magazine*, vol. 21, no. 3, pp. 41–50, 2014.
- [11] H. Cao, Y. Li, C. Liu, and S. Zhao, "ESO-based robust and high-precision tracking control for aerial manipulation," *IEEE Transactions on Automation Science and Engineering*, vol. 21, no. 2, pp. 2139–2155, 2023.
- [12] H. Yang and D. Lee, "Dynamics and control of quadrotor with robotic manipulator," in *2014 IEEE International Conference on Robotics and Automation (ICRA)*, pp. 5544–5549, IEEE, 2014.
- [13] J. Welde, J. Paulos, and V. Kumar, "Dynamically feasible task space planning for underactuated aerial manipulators," *IEEE Robotics and Automation Letters*, vol. 6, no. 2, pp. 3232–3239, 2021.
- [14] P. Chermprayong, K. Zhang, F. Xiao, and M. Kovac, "An integrated Delta manipulator for aerial repair: A new aerial robotic system," *IEEE Robotics & Automation Magazine*, vol. 26, no. 1, pp. 54–66, 2019.
- [15] M. Sánchez, J. Á. Acosta, and A. Ollero, "Integral action in first-order closed-loop inverse kinematics. application to aerial manipulators," in *2015 IEEE international conference on robotics and automation (ICRA)*, pp. 5297–5302, IEEE, 2015.
- [16] L. Sciavicco, L. Villani, B. Siciliano, and G. Oriolo, *Robotics: modelling, planning and control*. Springer, 2010.
- [17] P. Chiacchio, S. Chiaverini, L. Sciavicco, and B. Siciliano, "Closed-loop inverse kinematics schemes for constrained redundant manipulators with task space augmentation and task priority strategy," *The International Journal of Robotics Research*, vol. 10, no. 4, pp. 410–425, 1991.
- [18] G. Muscio, F. Pierri, M. A. Trujillo, E. Cataldi, G. Antonelli, F. Caccavale, A. Viguria, S. Chiaverini, and A. Ollero, "Coordinated control of aerial robotic manipulators: theory and experiments," *IEEE Transactions on Control Systems Technology*, vol. 26, no. 4, pp. 1406–1413, 2017.
- [19] D. Lunni, A. Santamaría-Navarro, R. Rossi, P. Rocco, L. Bascetta, and J. Andrade-Cetto, "Nonlinear model predictive control for aerial manipulation," in *2017 International Conference on Unmanned Aircraft Systems (ICUAS)*, pp. 87–93, IEEE, 2017.
- [20] D. Lee, H. Seo, D. Kim, and H. J. Kim, "Aerial manipulation using model predictive control for opening a hinged door," in *2020 IEEE International Conference on Robotics and Automation (ICRA)*, pp. 1237–1242, IEEE, 2020.
- [21] E. Cataldi, F. Real, A. Suárez, P. Di Lillo, F. Pierri, G. Antonelli, F. Caccavale, G. Heredia, and A. Ollero, "Set-based inverse kinematics control of an anthropomorphic dual arm aerial manipulator," in *2019 International Conference on Robotics and Automation (ICRA)*, pp. 2960–2966, IEEE, 2019.
- [22] Y. Chen, L. Lan, X. Liu, G. Zeng, C. Shang, Z. Miao, H. Wang, Y. Wang, and Q. Shen, "Adaptive stiffness visual servoing for unmanned aerial manipulators with prescribed performance," *IEEE Transactions on Industrial Electronics*, vol. 71, no. 9, pp. 11028–11038, 2024.
- [23] W. Shi, C. Keliris, M. Hou, G. Duan, and M. M. Polycarpou, "Preset-trajectory-based tracking control of a class of mismatched uncertain systems," *IEEE Transactions on Automatic Control*, vol. 70, no. 1, pp. 526–533, 2025.
- [24] M. López, E. Castillo, G. García, and A. Bashir, "Delta robot: inverse, direct, and intermediate Jacobians," *Proceedings of the Institution of Mechanical Engineers, Part C: Journal of Mechanical Engineering Science*, vol. 220, no. 1, pp. 103–109, 2006.
- [25] J. E. Shigley, C. R. Mischke, and T. H. Brown Jr, *Standard handbook of machine design*. McGraw-Hill Education, 2004.
- [26] H. K. Khalil, *Nonlinear systems*, vol. 3. Prentice hall Upper Saddle River, NJ, 2002.
- [27] B. Stellato, G. Banjac, P. Goulart, A. Bemporad, and S. Boyd, "OSQP: an operator splitting solver for quadratic programs," *Mathematical Programming Computation*, vol. 12, no. 4, pp. 637–672, 2020.
- [28] K. Baizid, G. Giglio, F. Pierri, M. A. Trujillo, G. Antonelli, F. Caccavale, A. Viguria, S. Chiaverini, and A. Ollero, "Behavioral control of unmanned aerial vehicle manipulator systems," *Autonomous Robots*, vol. 41, no. 5, pp. 1203–1220, 2017.
- [29] S. Zhao, *Mathematical Foundations of Reinforcement Learning*. Springer Nature Press, 2025.